Wannier charge center, spin resolved bulk polarization, and corner modes in a strained quantum spin Hall insulator

Srijata Lahiri and Saurabh Basu
Department of Physics, Indian Institute of Technology Guwahati-Guwahati, 781039 Assam, India

(Received 27 November 2023; revised 10 February 2024; accepted 1 March 2024; published 18 March 2024)

Topological invariants are a significant ingredient in the study of topological phases of matter that intertwines the supposedly contradicting concepts of bulk and boundary. The nature of the invariants differs depending on the dimensionality of the boundary at which the topologically nontrivial states manifest themselves. The primary motivation of this work is to study two distinct scenarios of topological phases, differing in the dimensionality of their boundary states, and study the associated bulk topological invariants that characterize them. In this regard, we study the band-engineered Kane-Mele model which originally is a prototypical example of a system that hosts quantum spin Hall effect on a honeycomb lattice. Under a smooth band deformation caused by varying one of the nearest-neighbor hopping amplitudes (say t_1) as compared to the other two (say t), we observe that the system transits from its first-order topological insulating state (or quantum spin Hall state) to a second-order topological insulating (SOTI) state via a gap-closing transition. This transition occurs when the system crosses a particular threshold of the deformation parameter t_1/t (namely, $t_1/t = 2$), known as the semi-Dirac limit in literature. We show the presence of edge and corner modes as a signature of first- and second-order topology, respectively. Further, we observe the evolution of the Wannier charge center (WCC), a bulk property as a function of the deformation parameter t_1/t. It is seen that the behavior of the WCC is entirely different in the quantum spin Hall (QSH) phase as compared to the second-order topological state. We also find that, while the $\mathbb{Z}_2$ invariant successfully characterizes the QSH state, it cannot characterize higher-order topology (second order here). The model being mirror invariant, we also calculate mirror winding number to show that it is rendered trivial in the SOTI phase as well, while being nontrivial in the QSH phase. Finally, we observe that the spin resolved bulk polarization correctly establishes the appearance of second-order topological corner modes and thus categorizes this phase as an *obstructed atomic insulator*.

DOI: 10.1103/PhysRevB.109.115424

I. INTRODUCTION

Topological insulators (TI) have been a subject of extensive research in the past decade. TIs are novel materials that show the intriguing feature of hosting a gapped bulk, but gapless edge and surface states. These topological states are robust and protected against minor perturbations that do not disturb the symmetries inherent in the system. Traditional TIs show the essence of nontrivial topology on a $(d-1)$-dimensional surface for a bulk that is d dimensional [1–5]. A major aspect of topological materials lies in the bulk boundary correspondence, where a topological invariant, evaluated purely from the bulk eigenstates, predicts the behavior at the boundaries of the system. Currently, there have been multiple extensions to the field of topological materials. These include Floquet topological insulators which exhibit topological phases exclusive to a periodically driven system and not shown by their static counterpart [6–9]. Furthermore, non-Hermitian (NH) TIs are gaining growing attention recently [10–14]. Non-Hermiticity enhances the richness of topological phases of matter and cannot be bound within the conventional *10-fold classification* of symmetry-protected topological states. NH systems also feature topological manifestations unusual to their Hermitian counterparts which include the presence of exceptional points and skin effect. Another important extension to the field of topological insulators, that is being actively explored, are higher-order topological insulators (HOTI) [9,15–33]. Unlike conventional TI, an nth-order HOTI exhibits the presence of nontrivial topological states on a surface or edge of dimension $d-n$ for a bulk that is d dimensional. This gives rise to corner modes in two dimensions (2D) and corner or hinge modes in three-dimensional (3D) HOTI systems. The conventional definition of bulk boundary correspondence fails here. Rather, HOTI shows a refined bulk boundary correspondence. Higher-order topological insulators can be majorly called a "subclass" of topological crystalline insulators where rotation or mirror symmetries protect the topological phases. Research in this field found a massive boost with the advent of the electric multipole insulators in the study of Benalcazar *et al.* [34] as well as chiral and helical higher-order topological states in the study of Schindler *et al.* [35]. In the latter work, prospective material candidates such as SnTe and surface modified BiTe and BiSe have been theoretically claimed to host a higher-order phase. However, despite HOTI being a well-studied phenomenon in recent times, it is still ambiguous how the topological conducting edge and surface states of a 2D and 3D system can be gapped out to show higher-order topology. Here, we study one such possibility where band deformation under strain of a quantum spin Hall insulator induces a transition from a TI to an HOTI phase of matter.

Our primary aim is to study two topological phases of different order, one evolving into the other and track the behavior of the corresponding bulk topological invariants that characterize them. In this regard, the Kane-Mele model, which is a prototypical example of the quantum spin Hall insulator, is considered [36]. The proposal of the Kane-Mele model owes its origin to the seminal work by Haldane who showed that an external magnetic field and hence Landau levels are not indispensable for the observation of quantum Hall effect [37]. Haldane introduced a complex second-neighbor hopping to a honeycomb lattice which causes the Dirac nodes at the **K** and **K**′ points in the Brillouin zone (BZ) of bare graphene to gap out, thus giving rise to conducting edge states. This complex second-neighbor hopping. however, breaks time-reversal symmetry (TRS) and bestows the occupied energy subspace with a nonzero Chern number, thus yielding a nonzero conductance similar to the original quantum Hall effect. Since the Haldane model breaks TRS, it was now imperative to study how topology behaves if TRS is restored. With this aim, Kane and Mele proposed a spinful model with an equal and opposite Haldane flux for the spin-up and -down particles. The spinful bands acquire opposite Chern number, thus causing the net Chern number of the occupied energy subspace to vanish. This is in accordance with TRS. It is, however, observed that the difference of Chern number for the two spin sectors acts as an effective topological invariant implying that the system shows a finite spin Hall conductance although the conductance in the charge sector vanishes. Such systems fall under the class of $\mathbb{Z}_2$ topological insulators and show the presence of helical edge states. Moreover, it was observed by Kane and Mele that an inversion-symmetry-breaking Rashba spin-orbit coupling term, that destroys the conservation of the z component of spin, causes little qualitative difference to the original results owing to leaving the TRS intact. Experimental evidence of the QSH state has been suggested to be found in HgTe/CdTe quantum well [38], low buckled germanene [39], Cl-doped ZnSe [40], Pt wires [41], etc.

Owing to the intriguing topological aspects of graphene, it has been the subject of intense study under various perturbations, one of them being strain. Several works have studied different aspects of strained graphene as well as the Haldane model, to show how the topological attributes of the system change. In the work by Murakami *et al.* [42], the jump in polarization as a function of a symmetry-breaking mass term is studied. This jump corresponds to the existence of a Weyl node at vanishing mass, at which the polarization is no longer defined. Second-order topology in a strained Haldane model has also been studied by Wang *et al.* [43]. Here the topological properties are observed as a function of change in both the nearest- and the next-nearest-neighbor hopping amplitudes. Corner modes are obtained as the deformation parameter exceeds a certain critical value. Another study by Liu *et al.* [44] explores the boundary states in pristine graphene sample under uniaxial strain and a correspondence with the SSH model is established. A very significant work in this direction has also been done by Ezawa *et al.* [45], where Wannier-type higher-order topological insulators have been discussed. The emergence of corner states is observed in a strained honeycomb lattice in 2D and diamond lattice in 3D. The topological origin of these second-order states is further explained via the

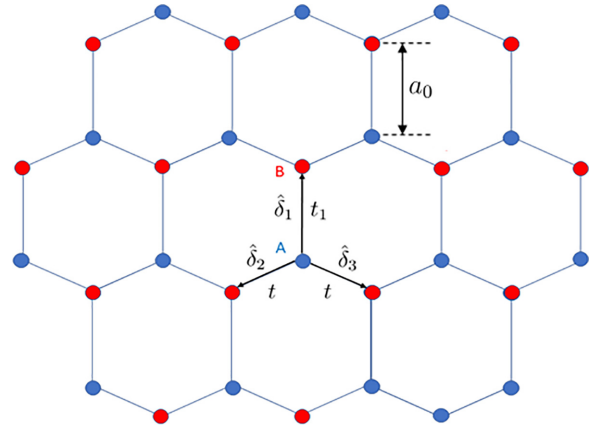

FIG. 1. A schematic representation of the honeycomb lattice on which the Kane-Mele model is studied. $\hat{\delta}_1$, $\hat{\delta}_2$, and $\hat{\delta}_3$ represent nearest-neighbor vectors. a_0 represents the nearest-neighbor distance.

bulk polarization calculated in accordance with the modern theory of polarization. In this work, we similarly deform the bands of the Kane-Mele model defined on a honeycomb lattice by modifying one of the nearest-neighbor hopping amplitudes (say t_1), while keeping the other two (say t) fixed (Fig. 1). It is seen that the quantum spin Hall state with distinct edge modes is destroyed beyond the critical point $t_1/t = 2$, and the system converts itself into a second-order topological insulator, which is an HOTI with topological states manifested at the $(d-2)$-dimensional boundary. The bulk band structure shows a shift in the band extrema points as a function of the deformation parameter $\xi = t_1/t$. At $t_1 = t$ $(\xi = 1)$ the bulk band structure hosts the band minima at the **K** and **K**′ points in the Brillouin zone (BZ). The band minima of the energy spectra shift towards each other along the Γ-**K**-**M**-**K**′-Γ line (Fig. 2) before finally merging at the **M** point of the BZ when $t_1 = 2t$ $(\xi = 2)$. It should be mentioned here that the limit

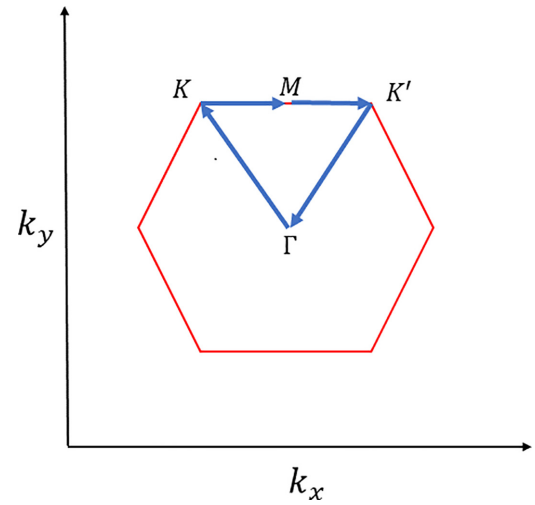

FIG. 2. The Brillouin zone corresponding to the honeycomb lattice is shown here. Γ, **K**, **M**, and **K**′ represent high-symmetry points of the honeycomb lattice. The band structures are studied along the Γ-**K**-**M**-**K**′-Γ line, which is shown by arrows.

$t_1 / t = 2$ is largely known as the semi-Dirac limit, where the bulk energy spectrum shows a linear dispersion along one component of momentum and a quadratic dispersion along the direction perpendicular to the former. Evidence of such inhomogeneous dispersion has been expected to be found in monolayer phosphorene subjected to pressure or doping [46], deformed graphene [47], etc. It is seen that the behavior of the bulk topological invariants corresponding to the two different topological regimes (that is, $\xi < 2$ and $\xi > 2$) are completely different owing to their dissimilar order. In this regard, we mention another work by Ren *et al.* [48], where an in-plane Zeeman field applied to the Kane-Mele model destroys the QSH phase and transforms the system into a higher-order topological insulator. However, the TRS is broken in this system and the vital essence of the Kane-Mele model is lost. On the contrary, in our work we keep the TRS of the system undisturbed while inducing a second-order topological phase solely by means of band engineering. While extensive work has been done on several models featuring an HOTI phase, we focus on the transition of the system and the corresponding bulk topological invariants as it smoothly changes its topological order as a function of band deformation. We also provide a clear perspective pertaining to the occurrence of this transition which is crucial to the study of topological phases of matter.

The paper is organized as follows. In Sec. II we define the tight-binding Hamiltonian for the strained Kane-Mele model and show the effect of band deformation on the bulk band structure. The energy spectra of a ribbonlike configuration are also studied which shows the existence of helical edge modes in the regime $\xi < 2$. Further deformation destroys the QSH phase and the helical edge modes vanish. However, beyond this critical point, a real-space probability distribution shows the existence of zero-energy corner modes in the system localized at two corners of a suitably formed supercell that obey the crystal symmetries of the Hamiltonian. In Sec. III we study the evolution of the Wannier charge center along one direction with respect to momentum along the other (since our system is two dimensional). It is seen that the nature of this evolution is completely dissimilar for the two different regimes. Correspondingly, the $\mathbb{Z}_2$ invariant which is finite in the region $\xi < 2$ vanishes beyond it. Pertaining to the presence of mirror symmetry M_x in the system, we also calculate the mirror winding number which corresponds to the Berry phase picked up by the ground state of a mirror-symmetry resolved effective Hamiltonian over a complete cycle in its parameter space. We observe that the mirror winding number shows a similar trend as the WCC. However, the spin resolved bulk polarization which indicates the position of the center of charge in a unit cell becomes quantized in the second-order topological phase. This indicates an *obstructed atomic insulator* where the center of charge suffers a mismatch from the original lattice sites [49]. This leads to an excess charge accumulation at the corners of a rhombic supercell which manifests as second-order topology. Finally, we conclude with a brief summary of our results in Sec. IV.

II. THE HAMILTONIAN

The Kane-Mele model defined on a honeycomb lattice is shown in Fig. 1. The vectors connecting the nearest neighbors (NN) are given by $\vec{\delta}_1 = a_0(0, 1)$, $\vec{\delta}_2 = a_0(-\frac{\sqrt{3}}{2}, -\frac{1}{2})$, $\vec{\delta}_3 = a_0(\frac{\sqrt{3}}{2}, -\frac{1}{2})$, where a_0 is the nearest-neighbor distance. The lattice vectors are given by $\vec{a}_1 = \vec{\delta}_1 - \vec{\delta}_2$ and $\vec{a}_2 = \vec{\delta}_1 - \vec{\delta}_3$. The hexagonal lattice has two sublattices denoted by A and B. In our model, the NN hopping along the direction $\hat{\delta}_1$ is assumed to be t_1, while it is given by t in the directions $\hat{\delta}_2$ and $\hat{\delta}_3$. We tune the band structure as a function of the deformation parameter $\xi = \frac{t_1}{t}$ and observe the behavior of the boundary states. The tight-binding Hamiltonian for the real-space Kane-Mele model is given as

$$H = \sum_{\langle i,j\rangle} t_{ij} c_i^\dagger c_j + i\lambda_{\rm so} \sum_{\langle\langle i,j\rangle\rangle} \nu_{ij} c_i^\dagger \sigma_z c_j + i\lambda_R \sum_{\langle i,j\rangle} c_i^\dagger (\boldsymbol{\sigma} \times \hat{\mathbf{d}}_{\mathbf{ij}})_z c_j + \sum_i \lambda_v c_i^\dagger c_i, \tag{1}$$

where c_i ($c_i^\dagger$) represent annihilation (creation) operators at lattice site i. Here t_{ij} is the NN hopping amplitude which is equal to t_1 when the hopping occurs along the direction $\vec{\delta}_1$ and is equal to t along $\vec{\delta}_2$ and $\vec{\delta}_3$. The second term is a spin-orbit coupling (SOC) term where $\lambda_{\rm so}$ corresponds to the intrinsic SOC amplitude which is a key ingredient in the formation of the QSH phase. $\nu_{ij} = 1$ (-1) if the electron takes a left (right) turn while moving from site j to site i. The third term corresponds to Rashba SOC with λ_R as the coupling strength. The conservation of the z component of spin that is σ_z is violated in presence of λ_R. $\hat{\mathbf{d}}_{\mathbf{ij}}$ corresponds to the nearest-neighbor vector connecting site j to site i. Finally, the fourth term denotes the onsite sublattice potential where λ_v assumes a positive amplitude (say m_s) for sublattice A and negative (say $-m_s$) for sublattice B. It is known that the QSH phase survives in the original Kane-Mele as long as $\lambda_v < 3\sqrt{3}\lambda_{\rm so}$ [36]. Fourier transformation of the real-space Hamiltonian gives us the tight-binding Hamiltonian in the momentum space,

$$H(\mathbf{k}) = \begin{pmatrix} \gamma(\mathbf{k}) + m_s & \eta(\mathbf{k}) & 0 & \rho(\mathbf{k}) \\ \eta^*(\mathbf{k}) & -\gamma(\mathbf{k}) - m_s & -\rho(-\mathbf{k}) & 0 \\ 0 & -\rho^*(-\mathbf{k}) & -\gamma(\mathbf{k}) + m_s & \eta(\mathbf{k}) \\ \rho^*(\mathbf{k}) & 0 & \eta^*(\mathbf{k}) & \gamma(\mathbf{k}) - m_s \end{pmatrix}, \tag{2}$$

where

$$\eta(\mathbf{k}) = t_1 e^{-ik_y a_0} + 2te^{\frac{ik_y a_0}{2}} \cos\frac{\sqrt{3}k_x a_0}{2}, \tag{3a}$$

$$\gamma(\mathbf{k}) = 2\lambda_{\rm so}\left[2\sin\frac{\sqrt{3}k_x a_0}{2}\cos\frac{3k_y a_0}{2} - \sin\sqrt{3}k_x a_0\right], \tag{3b}$$

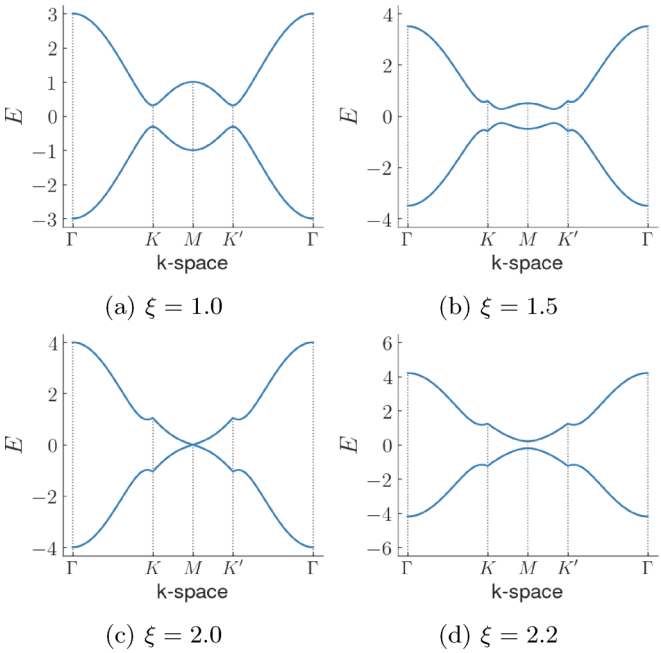

(a) $\xi = 1.0$ (b) $\xi = 1.5$

(c) $\xi = 2.0$ (d) $\xi = 2.2$

FIG. 3. The bulk band structure of the band-deformed Kane Mele model is shown for different values of the deformation parameter $\xi(=\frac{t_1}{t})$. It is seen that the band extrema shift towards each other as a function of ξ, to finally meet at the **M** point of the BZ for $\xi = 2$. As ξ is increased further, the gap reopens, indicating a topological phase transition. The values of λ_{so} are fixed at $0.06t$ while λ_R and λ_v are kept 0. This leads to a twofold degeneracy of the bulk bands.

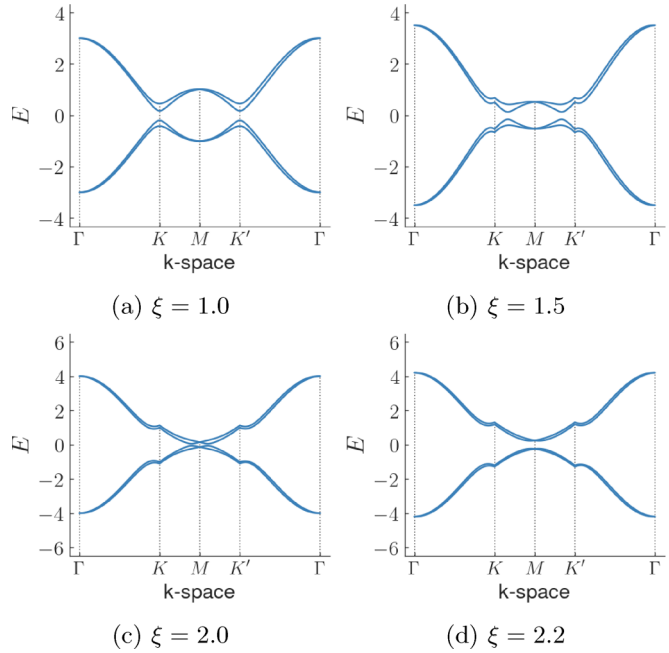

(a) $\xi = 1.0$ (b) $\xi = 1.5$

(c) $\xi = 2.0$ (d) $\xi = 2.2$

FIG. 4. The twofold degeneracy of the bulk band structure is lifted as soon as nonzero values of λ_R and λ_v are introduced in the model. The behavior of the bands with respect to the deformation parameter ξ, however, remains the same as shown in Fig. 3. Here, values of the parameters are given by $\lambda_{so} = 0.06t$, $\lambda_R = 0.05t$, and $\lambda_v = 0.1t$.

$$\rho(\mathbf{k}) = i\lambda_R\left[e^{-ik_y a_0} + e^{\frac{ik_y a_0}{2}} 2\cos\left(\frac{\sqrt{3}k_x a_0}{2} + \frac{\pi}{3}\right)\right]. \quad (3c)$$

The bulk band structure calculated using Eq. (2) shows band extrema at the $\mathbf{K}=(\frac{-2\pi}{3\sqrt{3}a_0}, \frac{2\pi}{3a_0})$ and $\mathbf{K}'=(\frac{2\pi}{3\sqrt{3}a_0}, \frac{2\pi}{3a_0})$ points for $\xi = \frac{t_1}{t} = 1$, as seen in Fig. 3. In this case the amplitude of the Rashba SOC and the onsite sublattice potential are kept zero resulting in the spin-↑ and spin-↓ bands to be degenerate. It is seen that as the band is slowly deformed, the extrema slowly shift towards each other, finally converging at the **M** point of the BZ for $\xi = 2$. The gap-closing transition at $\xi = 2$ destroys the QSH phase and renders the system trivial from the perspective of first-order topology. For nonzero values of the onsite potential λ_v and λ_{so}, the degeneracy of the bands is lifted as seen in Fig. 4. However, the general behavior of the spectral properties with respect to the deformation parameter remains the same. It is to be noted that in the absence of spin-orbit coupling (λ_{so} and λ_R) and an onsite potential (λ_v), the band degeneracy occurs at the point in the BZ given by

$$k_x = \pm\frac{2}{\sqrt{3}a_0}\cos^{-1}\left(\frac{t_1}{2t}\right), \quad (4a)$$

$$k_y = \frac{2\pi}{3a_0} \quad (4b)$$

for $1 < t_1 < 2$. In the presence of spin-orbit coupling, the degeneracy at these points are lifted and a topological gap opens up.

Next, in order to study the behavior of the edge modes pertaining to the QSH phase, we plot the energy band structure of a zigzag-ribbon-like configuration with periodic boundary condition (PBC) along the direction $\hat{a}_1 - \hat{a}_2$ and open boundary condition (OBC) along the direction $\hat{a}_1$. The presence of PBC along the x direction (which is the same as the direction $\hat{a}_1 - \hat{a}_2$) enables us to Fourier transform the Hamiltonian along the x direction and thus plot the dispersion of this finite ribbon as a function of k_x. Distinct edge modes are seen traversing the band gap as a function of k_x, in the region $1 < \xi < 2$, as shown in Fig. 5. Evidently, these are conducting eigenstates confined to the edges of the system. At $\xi = 2$, the closure of the bulk band gap causes the first-order topological phase to disappear and the conducting edge states get trivialized beyond this critical point.

To investigate the topology of the phase beyond the critical point ($\xi = 2$), we carefully construct a rhombic supercell taking into the account that the system possesses a mirror symmetry M_x. A schematic representation of this supercell is shown in Fig. 6. The real-space energy eigenspectra are evaluated which show the presence of four distinct zero-energy modes. In presence of a nonzero onsite potential λ_v, the in-gap modes shift from zero energy as shown in Fig. 7. The real-space probability distribution of the zero-energy states shows that they are confined at the two mirror-invariant corners of the rhombic supercell (Fig. 8).

III. TOPOLOGICAL INVARIANTS

The QSH phase seen in the regime $\xi < 2$ is a $\mathbb{Z}_2$ topological phase which has a zero Hall conductivity but a nonzero

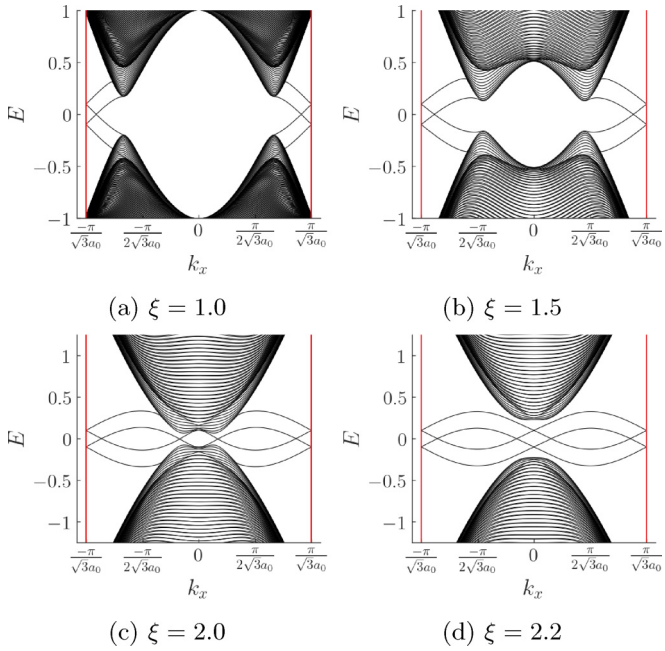

FIG. 5. The band structure of a finite zigzag-ribbon-like configuration for the deformed Kane-Mele model is shown. In (a) and (b) distinct helical edge states are seen traversing the band gap as long as $\xi < 2$. (c), (d) Show the scenario for $\xi = 2$ and beyond. We observe that beyond the critical value of deformation, the edge states do not traverse the band gap and hence carry no topological significance anymore. This indicates at a destruction of the QSH phase beyond the critical point.

spin Hall conductivity. If the z component of spin, that is σ_z, is conserved (for the case where $\lambda_R = 0$), the spin Hall conductivity is also quantized. The $\mathbb{Z}_2$ invariant in such a case

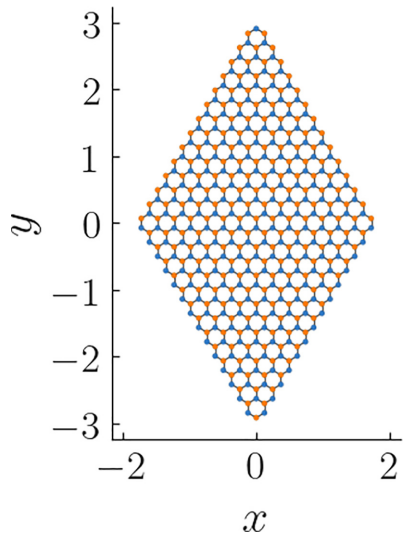

FIG. 6. A rhombic supercell constructed using the honeycomb lattice that is used in the calculations of the second-order topological phase. The x and y axes represent real-space position coordinates of the lattice sites in units of nm. The nearest-neighbor distance has been taken to be equal to 0.142 nm.

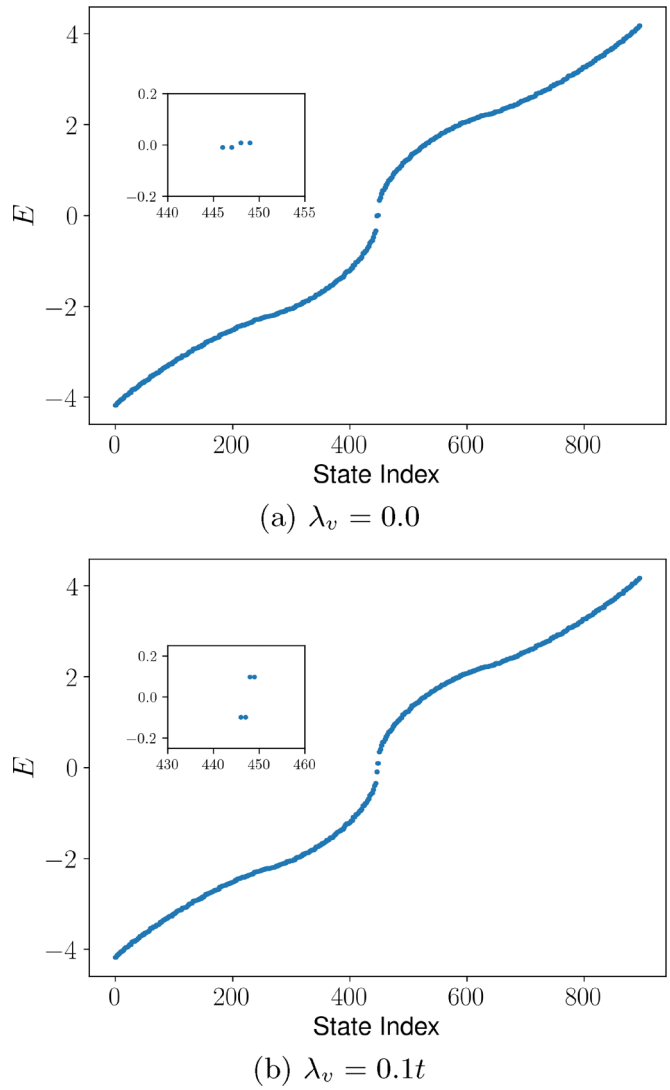

FIG. 7. The real-space energy eigenspectra are plotted for two different values of the Semenoff mass λ_v. The value of the deformation parameter is fixed at $\xi = 2.2$. Furthermore, the values of λ_{so} and λ_R are fixed at $0.06t$ and $0.05t$, respectively. (a) The presence of energy eigenstates, separated from the bulk and pinned at zero energy, is seen in the spectrum. These states are fourfold degenerate as long as the Semenoff mass λ_v is kept 0. (b) For $\lambda_v = 0.1t$, the inversion symmetry in the system is broken and the states shift from zero energy. The insets in (a) and (b) zoom in the vicinity of the region $E = 0$ and resolve the four states near zero energy.

is given by [50,51]

$$\nu = (C^{\uparrow} - C^{\downarrow})/2, \tag{5}$$

where $C^{\uparrow}$ ($C^{\downarrow}$) refers to the spin-↑ (spin-↓) Chern numbers. However, in presence of a Rashba SOC, the z component of spin that is σ_z is not conserved and hence this form of the $\mathbb{Z}_2$ invariant is no longer valid. However, a quantized $\mathbb{Z}_2$ invariant pertaining to a quantum spin Hall phase still persists. In our work we study the hybrid Wannier charge centers as a function of the deformation parameter ξ to follow the fate of the QSH phase in the presence of σ_z nonconserving terms. In this context, Wannier charge center refers to the center

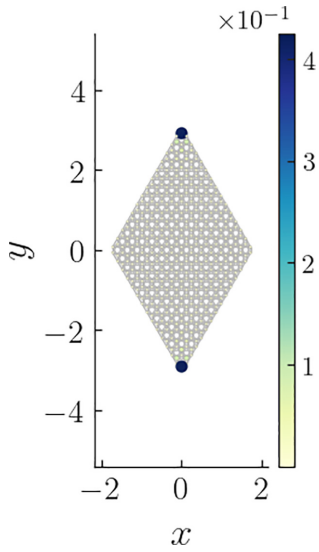

FIG. 8. Real-space probability density of one of the four degenerate zero-energy corner states is shown. The above plot is obtained for $\lambda_{so} = 0.06t$, $\lambda_R = 0.05t$, $\lambda_v = 0$, and $\xi = 2.2$. It is seen that the probability densities appear at the vertices. The details of the axes and the lattice spacing are the same as mentioned in Fig. 6.

of charge in a unit cell. Mathematically, they represent the expectation value of position operator for a basis represented by Wannier functions which are a set of orthogonal functions indexed by a lattice position, say **R**, and maximally localized about that point with respect to all relevant spatial dimensions. The Wannier functions are represented as [52]

$$|\mathbf{R}, n\rangle = \frac{V}{(2\pi)^D} \int d^D k\, e^{-i\mathbf{k}.\mathbf{R}} |\psi_{n\mathbf{k}}\rangle, \tag{6}$$

where $|\psi_{n\mathbf{k}}\rangle$ represents the Bloch wave function and D corresponds to the dimensionality of the k space. V is the real-space primitive cell volume. Hybrid Wannier functions, on the other hand, refer to wave functions which are localized along one spatial dimension (say x) while being delocalized along the other dimensions (say y and z) and can be written as

$$|R_x, k_y, k_z, n\rangle = \frac{1}{2\pi} \int_{-\pi}^{\pi} dk_x e^{-iR_x k_x} |\psi_{n\mathbf{k}}\rangle. \tag{7}$$

Expectation value of the position operator (say $\hat{\mathbf{X}}$) with respect to the hybrid Wannier function gives us the hybrid Wannier charge center. Mathematically, this is represented as

$$\bar{x}_n(k_y, k_z) = \langle R_x, k_y, k_z, n|\hat{\mathbf{X}}|R_x, k_y, k_z, n\rangle. \tag{8}$$

The hybrid WCC being proportional to the Berry phase captures the topological details of the system efficiently and is given as [53,54]

$$\bar{x}_n(k_y, k_z) = \frac{\phi_n(k_y, k_z)}{2\pi} = \frac{1}{2\pi} \int_0^{2\pi} A_n(k_x, k_y, k_z) dk_x \tag{9}$$

Here $\mathbf{A_n}(k_x, k_y, k_z) = -i\langle u_{n\mathbf{k}}|\nabla_{\mathbf{k}}|u_{n\mathbf{k}}\rangle$ is known as the Berry connection, where n is the band index and $|u_{n\mathbf{k}}\rangle$ corresponds to the periodic part of the Bloch wave function. Here, we perform hybrid Wannier transformation along the direction $\hat{b}_1$ and study its evolution as a function of the momentum in the direction $\hat{b}_2$ that is $k_{\hat{b}_2}$ (since the model we study is 2D and lies on the x-y plane) where $\vec{b}_1$ and $\vec{b}_2$ represent reciprocal lattice vectors of the honeycomb lattice and are given by

$$\vec{b}_1 = \left(\frac{2\pi}{a}, \frac{2\pi}{\sqrt{3}a}\right), \tag{10a}$$

$$\vec{b}_2 = \left(-\frac{2\pi}{a}, \frac{2\pi}{\sqrt{3}a}\right). \tag{10b}$$

Here, $a = \sqrt{3}a_0$ represents the smallest distance between similar sublattices. $k_{\hat{b}_1}$ and $k_{\hat{b}_2}$ correspondingly denote the momentum in the direction $\hat{b}_1$ and $\hat{b}_2$, respectively. Therefore, a general vector in the momentum space can be written as $\vec{k} = k_{\hat{b}_1}\hat{b}_1 + k_{\hat{b}_2}\hat{b}_2$. Correspondingly, we now calculate the Wannier charge center in the direction $\hat{a}_1$ as a function of the momentum variable in the direction $\hat{b}_2$ that is $k_{\hat{b}_2}$. Mathematically, this can be written as $\bar{r}^n_{\hat{a}_1} = \langle R_{\hat{a}_1}, k_{\hat{b}_2}, n|\hat{\mathbf{R}}_{\hat{a}_1}|R_{\hat{a}_1}, k_{\hat{b}_2}, n\rangle$, where $\hat{\mathbf{R}}_{\hat{a}_1}$ represents the position operator in the direction $\hat{a}_1$. In terms of the components of the Berry connection, the Wannier charge center can be written as

$$\bar{r}^n_{\hat{a}_1}(k_{\hat{b}_2}) = \frac{\phi_n(k_{\hat{b}_2})}{2\pi} = \frac{1}{2\pi} \oint A^n_{\hat{b}_1}(k_{\hat{b}_1}, k_{\hat{b}_2}) dk_{\hat{b}_1}. \tag{11}$$

Here $A^n_{\hat{b}_1}(k_{\hat{b}_1}, k_{\hat{b}_2}) = -i\langle u_{n\mathbf{k}}|\frac{\partial}{\partial k_{\hat{b}_1}}|u_{n\mathbf{k}}\rangle$. The $\mathbb{Z}_2$ invariant is now defined as the number of individual hybrid WCC crossed by a line traversing half the BZ, modulo 2 [55]. If the line cuts through odd (even) number of hybrid WCC while traversing half the BZ, the $\mathbb{Z}_2$ invariant is nontrivial (trivial). We observe in Fig. 9 that the $\mathbb{Z}_2$ invariant remains nontrivial as long as $\xi < 2$. Beyond this point, the evolution of the hybrid WCC is changed and the system no longer remains in the QSH phase, as shown in Fig. 10.

Next we focus on the crystalline symmetries of the deformed Kane-Mele Hamiltonian. The deformed Kane-Mele model possesses a mirror symmetry M_x given by $\sigma_x \otimes \mathbb{I}$, where σ_x and $\mathbb{I}$ act on the spin and the sublattice degrees of freedom, respectively. Here $\mathbb{I}$ corresponds to identity and σ_x corresponds to the x component of the Pauli matrices. The mirror symmetry decouples the Hamiltonian into two subspaces given by the positive and negative mirror eigenvalues. We set $k_x = 0$ and decouple the Hamiltonian $H(0, k_y)$ into two parts denoted by $H^{\pm}$ corresponding to the positive and the negative values of the mirror-symmetry operator M_x. The action of the mirror-symmetry operator on the Hamiltonian is given as follows:

$$M_x H(k_x, k_y) M_x^{-1} = H(-k_x, k_y). \tag{12}$$

Thus, on setting $k_x = 0$, the mirror operator M_x can be used to decouple the original Hamiltonian into $H^{\pm}$ which is given as

$$H^{\pm}(k_y) = T_x^{\pm}(k_y)\sigma_x + T_y^{\pm}(k_y)\sigma_y, \tag{13}$$

where

$$T_x^{\pm}(k_y) = \pm 2\lambda_R \sin\frac{3a_0 k_y}{2} + 4t\cos\frac{3a_0 k_y}{2} + 2t_1, \tag{14a}$$

$$T_y^{\pm}(k_y) = \pm 2\lambda_R\left[\cos\frac{3a_0 k_y}{2} + 1\right] - 4t\sin\frac{3a_0 k_y}{2}. \tag{14b}$$

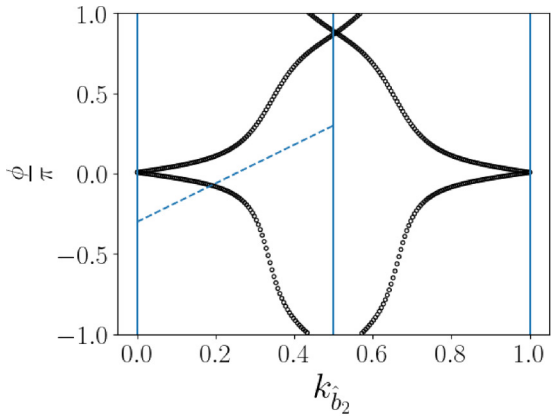

(a) $\xi = 1.0$

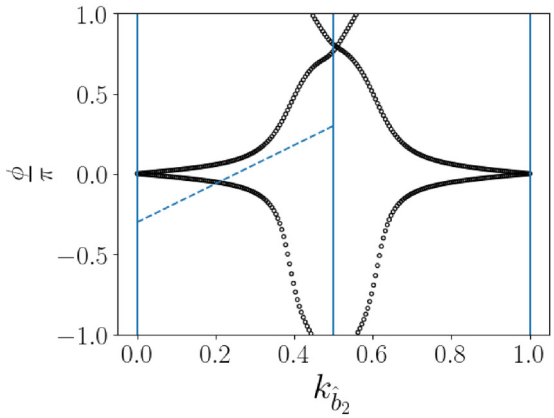

(b) $\xi = 1.5$

FIG. 9. Evolution of the Wannier charge center along the direction $\hat{a}_1$ as a function of $k_{\hat{b}_2}$ is shown for different values of the deformation parameter ξ in the QSH phase. Clearly, each WCC undergoes a winding as the value of $k_{\hat{b}_2}$ is evolved. The dotted line traversing half the BZ is an indicator of the $\mathbb{Z}_2$ invariant pertaining to the phase of the system. The number of intersections of the dotted line with the WCC curve denotes the $\mathbb{Z}_2$ invariant of the phase. All the calculations have been done for $\lambda_{so} = 0.06t$, $\lambda_R = 0.05t$, and $\lambda_v = 0.1t$. The horizontal axis has been scaled in units of $|\vec{b}_2|$. A mesh grid of size 200 has been used to discretize the $k_{\hat{b}_2}$ axis.

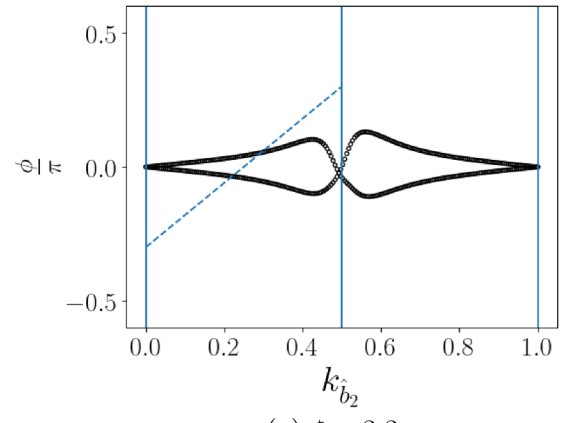

(a) $\xi = 2.2$

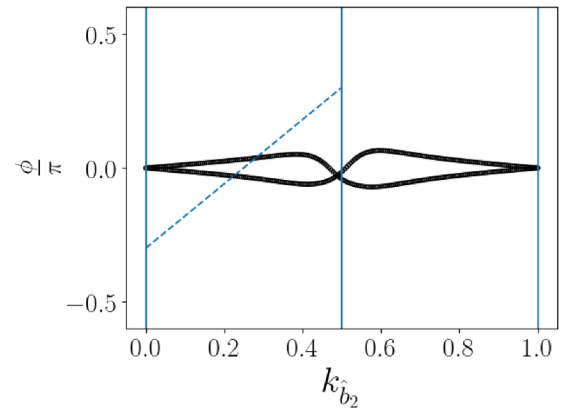

(b) $\xi = 2.5$

FIG. 10. Evolution of the Wannier charge center along $\hat{a}_1$ direction as a function of $k_{\hat{b}_2}$ is shown for different values of ξ in the SOTI phase. The two WCC undergo no winding here as a function of $k_{\hat{b}_2}$. Furthermore, the number of intersections of the dotted line traversing half the BZ with the two WCC is even. This indicates a trivial $\mathbb{Z}_2$ invariant. All the calculations have been done for $\lambda_{so} = 0.06t$, $\lambda_R = 0.05t$, and $\lambda_v = 0.1t$. The horizontal axis has been scaled in units of $|\vec{b}_2|$.

On studying the evolution of T_x and T_y over a complete path in the BZ ($\Gamma \to \mathbf{M} \to \Gamma$), we see that the winding number is 1 (that is the origin of the T_x-T_y plane is enclosed) only when the deformation parameter ξ remains less than 2. The origin lies outside the enclosed area as soon as the QSH phase is destroyed and the second-order topological phase is reached, as shown in Figs. 11(a)–11(c). This implies that the Berry phase acquired by the ground state of either the positive or negative subspace of the mirror resolved Hamiltonian is another alternate bulk property that correctly captures the QSH phase. However, it is trivial in the second-order topological regime. This has been shown in Fig. 11(d), where ϕ_m represents the Berry phase acquired by the ground state of the effective 1D mirror resolved Hamiltonian $H^+(k_y)$ over a complete 1D path in the BZ, and is given by

$$\phi_m = -i \int_{\Gamma \to M \to \Gamma} dk_y \langle u_{k_y} | \nabla_{k_y} | u_{k_y} \rangle. \tag{15}$$

$|u_{k_y}\rangle$ corresponds to the periodic part of the ground-state Bloch wave function $|\psi_{k_y}\rangle$ of the mirror resolved Hamiltonian $H^+(k_y)$. The negative mirror subspace given by $H^-(k_y)$ shows a similar behavior. Thus, it is implied that both the evolution of the WCC and the 1D polarization corresponding to the effective Hamiltonian $H^{\pm}(k_y)$ are incapable of capturing any essence of the second-order topological phase (that is the regime beyond $\xi > 2$) whereas they accurately characterize the first-order QSH phase.

To characterize the second-order topological states of the Kane-Mele model beyond $\xi > 2$, we resort to spin resolved bulk polarization. Keeping the value of $\lambda_R = 0$, so that the z component of spin is conserved, we calculate bulk polarization for the two different spin sectors which is given by [20]

$$p_\alpha^s = \bar{r}_\alpha = \langle w_n^s | r_\alpha | w_n^s \rangle = \frac{i}{S} \int_{\mathrm{BZ}} d^d k \langle u_{nk}^s | \frac{\partial}{\partial k_{r_\alpha}} | u_{nk}^s \rangle, \tag{16}$$

where $|w_n^s\rangle = |\mathbf{0}, n\rangle_s$ is the Wannier function corresponding to the nth band and p_α^s refers to the value of bulk polarization in the direction α for the spin component s ($\uparrow, \downarrow$). S

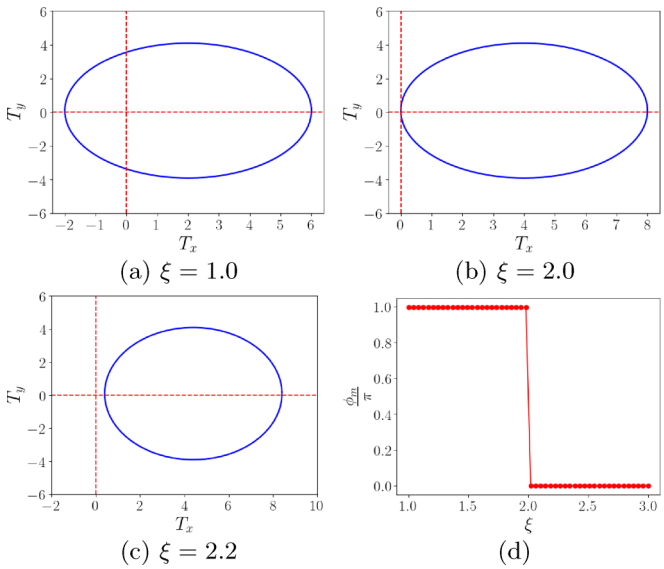

FIG. 11. The winding (or the absence of it) of the origin in the T_x-T_y plane of the positive mirror subspace is shown for several values of the deformation parameter ξ. (a) For $\xi = 1$ it seen that the origin lies within the area enclosed by the curve. (b) $\xi = 2$ clearly represents a phase transition (critical or gap-closing) point. (c) For $\xi > 2$, the origin is no longer wound. Due to the chiral symmetry of the mirror resolved Hamiltonian $H^{\pm}$, this winding directly corresponds to the Berry phase acquired by the corresponding eigenstate over a complete BZ. This winding number is plotted in (d) for a range of the deformation parameter ξ. It is seen that the 1D polarization or the Berry phase is incapable of characterizing the second-order topological phase. The values of the parameters have been kept fixed at $\lambda_{so} = 0.06t$, $\lambda_R = 0.05t$, and $\lambda_v = 0$.

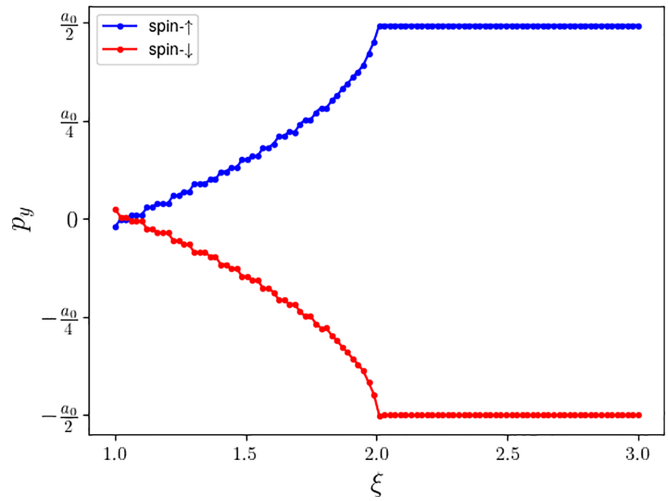

FIG. 12. The bulk polarization p_y^s has been plotted over a range of ξ. For the spin-↑ eigenstate, the bulk polarization acquires a quantized value of $\frac{a_0}{2}$ beyond $\xi > 2$, that is, in the SOTI phase. For the spin-↓ phase, the bulk polarization acquires a value of $-\frac{a_0}{2}$. The quantized value of bulk polarization indicates the formation of an *obstructed atomic insulator* where the center of charge does not coincide with the real lattice points. This gives rise to the formation of the SOTI phase. The values of the parameters are given by $\lambda_{so} = 0.06t$, $\lambda_R = 0$, and $\lambda_v \to 0$. A mesh grid of dimension $N_x \times N_y = 200 \times 200$ has been used to discretize the BZ.

corresponds to the total area of the honeycomb BZ and is taken as $8\pi^2 / 3\sqrt{3}a_0^2$. As shown in Fig. 12 we observe that the bulk polarization p_y^s has a quantized value of $\frac{a_0}{2}$ for the spin-↑ and a value of $-\frac{a_0}{2}$ for the spin-↓ component for the regime $\xi > 2$. For $1 < \xi < 2$, that is, in the QSH phase p_y^s bears no quantized value. Furthermore, it is seen that the value of p_x^s is uniformly zero both above and below the critical point $\xi = 2$. Thus, we establish that the second-order topological phase of the band-deformed Kane-Mele model is an *obstructed atomic insulator* phase where the center of charge in a unit cell is displaced from the actual lattice point in real space and lies between two consecutive sites. Such systems, where the center of charge is dislocated, exhibit the presence of localized boundary states when the system termination cuts through the charge center [56]. In our case, this phenomenon occurs at the corners of the rhombic supercell. This displacement of the center of charge thus results in fractional charge accumulation and hence exhibition of second-order topology in the form of localized corner modes.

A recent key experiment in the direction of our work has been done by Bampoulis *et al.* [39], where it has been shown that electric field induces a closing of the quantum spin Hall gap in germanene, thus destroying the topological phase. This is similar to the strain induced gap closure in the Kane-Mele model that we show in our paper. Germanene could be an ideal platform for the realization of our theoretical results, owing to the presence of a strong spin-orbit coupling, which is quite weak in graphene. Furthermore, in the work by Real *et al.* [57], the semi-Dirac dispersion was observed in a polariton honeycomb lattice. Optical lattices and metamaterials, which allow highly precise control over the system parameters, could also be excellent platforms for an extensive study on topology.

IV. CONCLUSION

We study a prototypical quantum spin Hall system that shows two topological phases of different orders, brought about by band deformation. The system under study is the celebrated Kane-Mele model on a honeycomb lattice which exhibits the presence of helical edge modes as a signature of the quantum spin Hall phase. We smoothly deform the band structure of the Kane-Mele model by varying one of the nearest-neighbor hopping amplitudes (say t_1) of the honeycomb lattice while keeping the other two (say t) fixed. It is observed that the system retains the QSH phase as long as $\frac{t_1}{t} < 2$. We plot the band structure of a zigzag-ribbon-like configuration to explicitly show the helical edge states which disappear after the system is deformed beyond $\frac{t_1}{t} = 2$. However, beyond this critical point is crossed, the system transcends into a second-order topological phase hosting robust second-order modes at the two corners of a suitably formed rhombic supercell. We study bulk properties like evolution of the hybrid WCC, mirror winding number, and spin resolved bulk polarization to characterize and study the evolution of the different topological phases. The evolution of the hybrid WCC shows a stark contrast in the first- and second-order topological phases. The nature of the evolution establishes

that the $\mathbb{Z}_2$ invariant is nontrivial in the QSH phase, while being trivial in the HOTI phase. The mirror winding number shows a similar behavior where it is nontrivial only in the QSH phase. Finally, to decipher the origin of the second-order topological phase we calculate spin resolved bulk polarization which depicts the center of charge in a unit cell. We observe that for $\xi > 2$, the value of $|p_y^s|$ is quantized for both the spin sectors at $\frac{a_0}{2}$, while it is not quantized for $\xi < 2$. p_x^s, on the other hand, is uniformly zero everywhere. This quantization of the value of p_y^s indicates a displacement of center of charge with respect to the real-space lattice site and causes the appearance of fractional charge excess at the corners of the rhombic supercell. The bulk polarization p_y^s for the spin-↑ sector is $\frac{a_0}{2}$ while it is $-\frac{a_0}{2}$ for the spin-↓ sector. Herein lies the appearance of a second-order topological phase beyond $\xi > 2$ which is an obstructed atomic insulator.

[1] S. Murakami, Two-dimensional topological insulators and their edge states, J. Phys.: Conf. Ser. **302**, 012019 (2011).

[2] M. Z. Hasan and C. L. Kane, Colloquium: Topological insulators, Rev. Mod. Phys. **82**, 3045 (2010).

[3] F. Liu and K. Wakabayashi, Novel topological phase with a zero Berry curvature, Phys. Rev. Lett. **118**, 076803 (2017).

[4] C.-X. Liu, S.-C. Zhang, and X.-L. Qi, The quantum anomalous Hall effect: Theory and experiment, Annu. Rev. Condens. Matter Phys. **7**, 301 (2016).

[5] D. Zhu, B.-X. Li, and Z. Yan, Sublattice-sensitive Majorana modes, Phys. Rev. B **106**, 245418 (2022).

[6] V. D. Lago, M. Atala, and L. E. F. F. Torres, Floquet topological transitions in a driven one-dimensional topological insulator, Phys. Rev. A **92**, 023624 (2015).

[7] T. Kitagawa, E. Berg, M. Rudner, and E. Demler, Topological characterization of periodically driven quantum systems, Phys. Rev. B **82**, 235114 (2010).

[8] A. K. Ghosh, T. Nag, and A. Saha, Time evolution of Majorana corner modes in a floquet second-order topological superconductor, Phys. Rev. B **107**, 035419 (2023).

[9] A. K. Ghosh, G. C. Paul, and A. Saha, Higher order topological insulator via periodic driving, Phys. Rev. B **101**, 235403 (2020).

[10] Q. Lin, T. Li, L. Xiao, K. Wang, W. Yi, and P. Xue, Observation of non-Hermitian topological Anderson insulator in quantum dynamics, Nat. Commun. **13**, 3229 (2022).

[11] Y. Long, H. Xue, and B. Zhang, Non-hermitian topological systems with eigenvalues that are always real, Phys. Rev. B **105**, L100102 (2022).

[12] S. Lieu, Topological phases in the non-Hermitian Su-Schrieffer-Heeger model, Phys. Rev. B **97**, 045106 (2018).

[13] S. Bid, G. K. Dash, and M. Thakurathi, Non-Hermitian higher-order Weyl semimetal with surface diabolic points, Phys. Rev. B **107**, 165120 (2023).

[14] H. Gao, H. Xue, Z. Gu, T. Liu, J. Zhu, and B. Zhang, Non-Hermitian route to higher-order topology in an acoustic crystal, Nat. Commun. **12**, 1888 (2021).

[15] Y. Xue, H. Huan, B. Zhao, Y. Luo, Z. Zhang, and Z. Yang, Higher-order topological insulators in two-dimensional dirac materials, Phys. Rev. Res. **3**, L042044 (2021).

[16] X. L. Sheng, C. Chen, H. Liu, Z. Chen, Z. M. Yu, Y. X. Zhao, and S. A. Yang, Two-dimensional second-order topological insulator in graphdiyne, Phys. Rev. Lett. **123**, 256402 (2019).

[17] W. A. Benalcazar, B. A. Bernevig, and T. L. Hughes, Electric multipole moments, topological multipole moment pumping, and chiral hinge states in crystalline insulators, Phys. Rev. B **96**, 245115 (2017).

[18] Z. Song, Z. Fang, and C. Fang, $(d-2)$-dimensional edge states of rotation symmetry protected topological states, Phys. Rev. Lett. **119**, 246402 (2017).

[19] M. Ezawa, Magnetic second-order topological insulators and semimetals, Phys. Rev. B **97**, 155305 (2018).

[20] M. Ezawa, Higher-order topological insulators and semimetals on the breathing kagome and pyrochlore lattices, Phys. Rev. Lett. **120**, 026801 (2018).

[21] M. Costa, G. R. Schleder, C. M. Acosta, A. C. M. Padilha, F. Cerasoli, M. B. Nardelli, and A. Fazzio, Discovery of higher-order topological insulators using the spin Hall conductivity as a topology signature, npj Comput. Mater. **7**, 49 (2021).

[22] R. Noguchi, M. Kobayashi, Z. Jiang, K. Kuroda, T. Takahashi, Z. Xu, D. Lee, M. Hirayama, M. Ochi, T. Shirasawa, P. Zhang, C. Lin, C. Bareille, S. Sakuragi, H. Tanaka, S. Kunisada, K. Kurokawa, K. Yaji, A. Harasawa, V. Kandyba *et al.*, Evidence for a higher-order topological insulator in a three-dimensional material built from van der Waals stacking of Bismuth-Halide chains, Nat. Mater. **20**, 473 (2021).

[23] M. Jangjan and M. V. Hosseini, Topological properties of subsystem-symmetry-protected edge states in an extended quasi-one-dimensional dimerized lattice, Phys. Rev. B **106**, 205111 (2022).

[24] S. Mukherjee, M. Di Liberto, P. Öhberg, R. R. Thomson, and N. Goldman, Experimental observation of Aharonov-Bohm cages in photonic lattices, Phys. Rev. Lett. **121**, 075502 (2018).

[25] R. Jackiw and C. Rebbi, Solitons with fermion number $\frac{1}{2}$, Phys. Rev. D **13**, 3398 (1976).

[26] L. Fu, Topological crystalline insulators, Phys. Rev. Lett. **106**, 106802 (2011).

[27] A. K. Ghosh, T. Nag, and A. Saha, Floquet generation of a second-order topological superconductor, Phys. Rev. B **103**, 045424 (2021).

[28] S. Franca, J. van den Brink, and I. C. Fulga, An anomalous higher-order topological insulator, Phys. Rev. B **98**, 201114(R) (2018).

[29] B. Huang, Topological invariants for anomalous floquet higher-order topological insulators, Front. Phys. **18**, 13601 (2023).

[30] T. Peng, C.-B. Hua, R. Chen, Z.-R. Liu, D.-H. Xu, and B. Zhou, Higher-order topological anderson insulators in quasicrystals, Phys. Rev. B **104**, 245302 (2021).

[31] G. Usaj, P. M. Perez-Piskunow, L. E. F. Foa Torres, and C. A. Balseiro, Irradiated graphene as a tunable floquet topological insulator, Phys. Rev. B **90**, 115423 (2014).

[32] D. Zhu, M. Kheirkhah, and Z. Yan, Sublattice-enriched tunability of bound states in second-order topological insulators and superconductors, Phys. Rev. B **107**, 085407 (2023).

[33] M. Kheirkhah, D. Zhu, J. Maciejko, and Z. Yan, Corner- and sublattice-sensitive Majorana zero modes on the kagome lattice, Phys. Rev. B **106**, 085420 (2022).

[34] W. A. Benalcazar, B. A. Bernevig, and T. L. Hughes, Quantized electric multipole insulators, Science **357**, 61 (2017).

[35] F. Schindler, A. M. Cook, M. G. Vergniory, Z. Wang, S. S. P. Parkin, B. A. Bernevig, and T. Neupert, Higher-order topological insulators, Sci. Adv. **4**, eaat0346 (2018).

[36] C. L. Kane and E. J. Mele, Quantum spin Hall effect in graphene, Phys. Rev. Lett. **95**, 226801 (2005).

[37] F. D. M. Haldane, Model for a quantum Hall effect without landau levels: Condensed-matter realization of the "parity anomaly", Phys. Rev. Lett. **61**, 2015 (1988).

[38] B. A. Bernevig, T. L. Hughes, and S.-C. Zhang, Quantum spin Hall effect and topological phase transition in HgTe quantum wells, Science **314**, 1757 (2006).

[39] P. Bampoulis, C. Castenmiller, D. J. Klaassen, J. van Mil, Y. Liu, C.-C. Liu, Y. Yao, M. Ezawa, A. N. Rudenko, and H. J. W. Zandvliet, Quantum spin Hall states and topological phase transition in germanene, Phys. Rev. Lett. **130**, 196401 (2023).

[40] N. P. Stern, S. Ghosh, G. Xiang, M. Zhu, N. Samarth, and D. D. Awschalom, Current-induced polarization and the spin Hall effect at room temperature, Phys. Rev. Lett. **97**, 126603 (2006).

[41] M. Isasa, E. Villamor, L. E. Hueso, M. Gradhand, and F. Casanova, Temperature dependence of spin diffusion length and spin Hall angle in Au and Pt, Phys. Rev. B **91**, 024402 (2015).

[42] H. Yoshida, T. Zhang, and S. Murakami, Polarization jumps by breaking symmetries of two-dimensional Weyl semimetals, Phys. Rev. B **107**, 035122 (2023).

[43] B. Wang, X. Zhou, H. Lin, and A. Bansil, Higher-order topological insulator phase in a modified Haldane model, Phys. Rev. B **104**, L121108 (2021).

[44] F.-F. Liu, Z.-F. Liu, Q.-P. Wu, W.-Y. Li, and X.-B. Xiao, Localized states induced by uniaxial strain in graphene quantum dots, Phys. E (Amsterdam) **149**, 115664 (2023).

[45] M. Ezawa, Minimal models for Wannier-type higher-order topological insulators and phosphorene, Phys. Rev. B **98**, 045125 (2018).

[46] A. S. Rodin, A. Carvalho, and A. H. C. Neto, Strain-induced gap modification in black phosphorus, Phys. Rev. Lett. **112**, 176801 (2014).

[47] G. Montambaux, F. Piéchon, J.-N. Fuchs, and M. O. Goerbig, Merging of dirac points in a two-dimensional crystal, Phys. Rev. B **80**, 153412 (2009).

[48] Y. Ren, Z. Qiao, and Q. Niu, Engineering corner states from two-dimensional topological insulators, Phys. Rev. Lett. **124**, 166804 (2020).

[49] B. Bradlyn, L. Elcoro, J. Cano, M. G. Vergniory, Z. Wang, C. Felser, M. I. Aroyo, and B. A. Bernevig, Topological quantum chemistry, Nature (London) **547**, 298 (2017).

[50] D. N. Sheng, Z. Y. Weng, L. Sheng, and F. D. M. Haldane, Quantum spin-hall effect and topologically invariant chern numbers, Phys. Rev. Lett. **97**, 036808 (2006).

[51] D. N. Sheng, L. Balents, and Z. Wang, Phase diagram for quantum Hall bilayers at $\nu = 1$, Phys. Rev. Lett. **91**, 116802 (2003).

[52] G. H. Wannier, The structure of electronic excitation levels in insulating crystals, Phys. Rev. **52**, 191 (1937).

[53] M. Taherinejad, K. F. Garrity, and D. Vanderbilt, Wannier center sheets in topological insulators, Phys. Rev. B **89**, 115102 (2014).

[54] A. A. Soluyanov and D. Vanderbilt, Wannier representation of $\mathbb{Z}_2$ topological insulators, Phys. Rev. B **83**, 035108 (2011).

[55] D. Gresch, G. Autès, O. V. Yazyev, M. Troyer, D. Vanderbilt, B. A. Bernevig, and A. A. Soluyanov, Z2Pack: Numerical implementation of hybrid Wannier centers for identifying topological materials, Phys. Rev. B **95**, 075146 (2017).

[56] S. Lahiri and S. Basu, Second order topology in a band engineered chern insulator, Sci. Rep. **14**, 1880 (2024).

[57] B. Real, O. Jamadi, M. Milićević, N. Pernet, P. St-Jean, T. Ozawa, G. Montambaux, I. Sagnes, A. Lemaître, L. Le Gratiet, A. Harouri, S. Ravets, J. Bloch, and A. Amo, Semi-dirac transport and anisotropic localization in polariton honeycomb lattices, Phys. Rev. Lett. **125**, 186601 (2020).